fire

MDPI

Article

Performance Optimization of Methanol Piezoelectric Injectors and Compression-Ignition Engines

Luan Zang [1,2], Mingzhou Liu [1], Yangyi Wu [3,*], Hongyan Zhu [2], Yueqi Han [4], Wei Gao [2], Jingrui Li [5] and Haifeng Liu [5]

[1] School of Mechanical Engineering, Hefei University of Technology, Hefei 230009, China
[2] FAW Wuxi Fuel Injection Equipment Research Institute, Wuxi 214063, China
[3] FAW Jiefang Automobile Co., Ltd. Wuxi Diesel Engine Factory, Wuxi 214026, China
[4] AECC Shenyang Liming Aero-Engine Co., Ltd., Shenyang 110041, China
[5] State Key Laboratory of Engines, Tianjin University, Tianjin 300072, China; haifengliu@tju.edu.cn (H.L.)
* Correspondence: yangyiwu@tju.edu.cn

Abstract

This study presented a comprehensive optimization of a piezoelectric injector specifically designed for pure methanol compression-ignition engines. As a fuel for compression-ignition engines, methanol exhibits broad application prospects. To overcome the challenges posed by methanol's low cetane number and energy density, a co-optimization strategy was implemented, targeting the actuator, drive waveform, and internal flow geometry. The redesigned injector exhibited superior dynamic performance, featuring significantly faster response times and enhanced operational stability, which were critical for precise fuel delivery control. Furthermore, the optimized internal flow path increased the effective flow rate, ensuring sufficient fuel supply across all engine operating conditions. The upgraded injector was rigorously tested on an engine bench, demonstrating substantial performance gains. Brake thermal efficiency improved from 38.9% to 40.4% at low load and from 43.68% to 46.07% at high load. Emissions of CO, formaldehyde, acetaldehyde, and unburned methanol were consistently reduced, with the maximum reduction reaching 23.1%, confirming markedly enhanced combustion completeness. This improvement was directly attributed to the injector's refined spray characteristics and precise control, although it led to a slight increase in NOx emissions due to higher peak combustion temperatures.

Keywords: injector; hydraulic amplifier; methanol engine; performance improvement; emissions

Check for updates

Academic Editor: Jiaqiang E

Received: 29 May 2026
Revised: 27 June 2026
Accepted: 30 June 2026
Published: 7 July 2026

Copyright: © 2026 by the authors. Licensee MDPI, Basel, Switzerland. This article is an open access article distributed under the terms and conditions of the Creative Commons Attribution (CC BY) license.

1. Introduction

As the cornerstone of modern industry and transportation, the Internal Combustion Engine (ICE) has long played a pivotal role on a global scale. The extensive application of ICEs across diverse sectors—ranging from automobiles, heavy-duty trucks, and marine vessels to aircraft and construction machinery—has been instrumental in the efficient functioning of human society [1,2]. Underpinned by high energy conversion efficiency, robust power output, and a mature technological framework, ICEs not only sustain modern mobility but also provide the prime power for the heavy industry, agriculture, and construction, thereby fostering global economic development and social progress [3–5]. Compared to alternative powertrain systems, ICEs offer superior energy density, delivering stable and sustained power. This advantage is particularly pronounced in heavy-duty transportation and machinery requiring prolonged operation under high-load conditions.

Furthermore, characterized by a relatively simple architecture, low maintenance costs, and a well-established global industrial chain with comprehensive supporting infrastructure, ICEs maintain ubiquitous application worldwide.

However, the ubiquity of internal combustion engines has precipitated significant environmental challenges, most notably the pollutant emissions intrinsically linked to fossil fuel combustion. Conventional ICEs rely predominantly on petroleum-derived fuels such as gasoline and diesel, which release substantial quantities of pollutants during combustion, primarily carbon dioxide (CO_2), nitrogen oxides (NOx), carbon monoxide (CO), and soot [6–8]. These emissions not only severely degrade air quality—contributing to the formation of haze and acid rain—but also accelerate the trajectory of global climate change. Specifically, the emission of NOx and soot poses direct risks to air quality and is epidemiologically associated with a range of respiratory and cardiovascular diseases, raising critical public health concerns. Consequently, the environmental footprint of traditional ICEs has garnered widespread societal attention, compelling governments worldwide to implement increasingly stringent emission standards and environmental regulations [9,10]. Furthermore, CO_2 emissions, as a primary constituent of greenhouse gases, are widely recognized as a key driver of global climate change. Excessive CO_2 discharge not only exacerbates global warming but also exerts profound negative impacts on ecological systems, climate patterns, and biodiversity [11,12]. Thus, while ICEs provide high-efficiency power, they simultaneously present a formidable challenge for environmental governance. In this context, compression-ignition (CI) engines are widely employed as primary power sources in automotive and construction machinery due to their superior fuel economy and reliability. In response to escalating energy crises and environmental concerns, advanced technologies such as high-pressure common rail (HPCR) fuel injection systems have been developed to meet stringent emissions regulations and societal demands. CI engines exhibit approximately 30% lower fuel consumption and about 45% lower CO_2 emissions compared to spark-ignition (SI) engines, underscoring their advantages in energy efficiency and environmental impact reduction [13,14].

Despite the significant advantages of CI engines in terms of CO_2 emissions and the fuel economy, their inherent challenges—specifically high NOx and soot emissions—have become a critical bottleneck under increasingly stringent global emission regulations [7,8]. To address these challenges and further unlock the potential for energy savings and emission reduction, innovation in advanced fuel injection technologies has emerged as a pivotal solution. Among these, the piezoelectric injector stands out due to its ultra-fast response speed, exceptional control precision, and flexible capability for multiple injections, offering an unprecedented means to optimize the combustion process. Compared to conventional solenoid-driven injectors, piezoelectric injectors enable microsecond-level actuation, allowing precise control over injection timing and quantity. This significantly enhances fuel atomization quality and air–fuel mixing, thereby achieving the dual objectives of reduced pollutant emissions and improved combustion efficiency. Consequently, a thorough investigation into the operational characteristics of piezoelectric injectors and their influence on the combustion process holds substantial theoretical and engineering significance for the development of next-generation clean and efficient CI engines [15–18].

In addition to optimizing the combustion process through advanced fuel injection systems, the development of clean and carbon-neutral alternative fuels represents another critical pathway to overcoming the environmental and resource constraints associated with conventional CI engines [19–24]. In this context, methanol has garnered significant attention in recent years due to its oxygenated molecular structure, ultra-low sulfur content, and potential for renewable production. Methanol can be synthesized from diverse feedstocks—including coal, natural gas, and biomass—and, more importantly, can be produced as

"green methanol" using renewable energy sources, thereby enabling substantial reductions in life-cycle greenhouse gas emissions and even achieving net-zero carbon operation [25,26]. Although methanol presents challenges in CI engines—notably its low cetane number and poor auto-ignition propensity—these limitations can be effectively mitigated through appropriate combustion strategies [22,27,28]. When properly implemented, methanol utilization significantly suppresses soot formation and markedly reduces emissions of sulfur oxides (SO_x) and soot to almost zero [27]. Shamun et al. [28] showed that pure methanol eliminated NOx-soot trade-off in PM emissions with diameters < 30 nm, minimally affected by injection pressure. Furthermore, through appropriate optimization, the brake thermal efficiency (BTE) of the methanol CI engine at a ultra-low load condition (below 10%) was significantly improved from 27.88% (original diesel baseline) to 30.21%, representing an increase of 8.4%. Additionally, the engine operated stably with a COVIMEP of less than 2 [29]. Consequently, investigating the mechanisms of efficient and clean methanol combustion in CI engines—and synergistically integrating it with advanced injection technologies—offers a highly promising avenue toward sustainable internal combustion power systems.

Methanol offers significant advantages in soot reduction and carbon neutrality, but its extremely low cetane number (typically below 5) and low volumetric energy density pose fundamental challenges to stable combustion in pure methanol CI engines. This observation was further corroborated by preliminary experiments conducted by our research team [29–31]. In the absence of a pilot fuel, methanol cannot reliably auto-ignite through compression heating alone and instead relies on a highly optimized in-cylinder thermodynamic environment coupled with precise fuel spray organization to initiate and sustain combustion [27–31]. This demands a fuel injection system capable of delivering a sufficient quantity of methanol into specific regions of the combustion chamber within an extremely short time window, thereby creating localized fuel-rich, high-temperature mixtures conducive to auto-ignition. Moreover, to compensate for the reduced energy input per cycle due to methanol's low calorific value, substantially higher fuel quantities must be injected per cycle, placing stringent requirements on injection metering accuracy and repeatability [31–39]. Conventional solenoid-driven injectors, limited by millisecond-scale response delays and restricted flexibility in multiple injection events, often fail to achieve the fine control over injection timing, pulse width, and spray development needed under transient operating conditions. This can lead to excessive ignition delay, misaligned combustion phasing, or even misfire [29–31]. Consequently, achieving efficient and stable combustion of pure methanol in CI mode necessitates an advanced injection system featuring microsecond-level dynamic response, high injection repeatability, and flexible multi-pulse capability—providing a clear technical rationale and compelling justification for the adoption of piezoelectric injectors in this context.

The foregoing analysis indicates that pure methanol CI engines impose exceptionally stringent demands on fuel injection systems in terms of dynamic response, metering accuracy, and long-term durability—challenges far exceeding those encountered with conventional fuels. These difficulties stem primarily from methanol's intrinsic physicochemical properties, including its low lower heating value (LHV), low cetane number, and low viscosity. Piezoelectric injectors, characterized by microsecond-level response times and high control flexibility, are widely recognized as a key enabling technology [40–42], having demonstrated significant contributions to improvements in both BTE and regulated/unregulated emissions [43–47]. Accordingly, this study employed piezoelectric injectors on an engine test bench to investigate in-cylinder high-pressure direct injection (HPDI) of methanol. Nevertheless, existing commercial injector designs exhibit notable deficiencies when applied to methanol, including insufficient actuator performance margin, poor adaptability of drive strategies, and internal flow-path geometries not optimized

for the elevated volumetric flow rates required for methanol combustion [29–31]. These limitations severely constrain the precise spray organization necessary across a wide operating range of methanol-fueled CI engines. To overcome these bottlenecks, systematic and coordinated optimization is urgently required across three critical domains: actuator hardware, drive control logic, and internal geometric configuration of the injector.

Accordingly, this study focused on targeted optimizations of key components of the piezoelectric injector—namely, the piezoelectric actuator, drive waveform, nozzle seat geometry, and the geometric profile of the displacement-amplifying piston within the internal hydraulic amplifier of the piezoelectric injector. The upgraded injector was integrated into a pure methanol CI engine and evaluated on an engine test bench. By comparing brake-specific fuel consumption (BSFC) and emission characteristics before and after the modifications, the effectiveness of the proposed improvements in enhancing both combustion performance and emissions was systematically assessed. This work provided a practical and viable technical pathway toward the engineering implementation of pure methanol CI, offering significant implications for the large-scale adoption of methanol fuel in CI engines.

2. Experimental Device, Method and Fuel

2.1. Experimental Device

To systematically evaluate the effects of piezoelectric injector performance improvements and the installation of methanol piezoelectric injectors on the overall performance of a CI engine, this study established a comprehensive experimental platform encompassing both component-level characterization and system-level validation. A straight-six, water-cooled, four-stroke, turbocharged and intercooled CI engine was employed as the test bench foundation. Furthermore, four specialized testing instruments were developed specifically for the core actuator of the piezoelectric injector: an electrical parameter tester, a hysteresis characteristic tester, a dynamic characteristic tester, and a stiffness tester. Specifically, the electrical parameter tester was utilized to accurately obtain the capacitance and dielectric loss tangent of the actuator, providing fundamental inputs for drive circuit design and control algorithm calibration. The hysteresis characteristic tester was employed to quantify the displacement nonlinearity of the actuator during voltage loading and unloading cycles, serving as a critical basis for optimizing multiple injection strategies and ensuring precise fuel delivery. The dynamic characteristic tester, utilizing non-contact laser displacement measurement, directly characterized the response time and effective displacement output capability of the actuator, thereby verifying core improvements such as reduced charging time and increased flow rate. The stiffness tester simulated high-pressure fuel reaction forces to determine the force–displacement characteristics of the actuator under varying mechanical loads, ensuring that effective displacement does not degrade under high-rail-pressure conditions and providing prerequisite validation for the reliability of thermal efficiency improvement data under high-load operations. Collectively, these instruments and the engine test bench constitute a closed-loop verification system spanning the fundamental physical characteristics of the injector to the overall combustion and emission performance of the engine, providing robust hardware support for the reliability of subsequent performance and emission data. The specific technical parameters of the injector testing equipment and the engine test bench are presented in Tables 1 and 2, respectively. The experimental setup diagram is shown as Figure 1.

It should be noted that the engine is equipped with a built-in 5 kW rated intake air heater, which activates during startup and operates at loads below 30%, and automatically deactivates when the engine load exceeds 30%.

Table 1. Main Technical Parameters of Core Testing Equipment for Piezoelectric Injectors.

Testing Equipment	Key Parameter	Technical Specification
Electrical Parameter Tester	Capacitance Measurement	1 pF–1 F
	Dielectric Loss Tangent Measurement	0.0001–9.9999
	Maximum Test Frequency	100 kHz
	Measurement Accuracy	≈0.1%
Hysteresis Characteristic Tester	Maximum Test Voltage	200 V
	Maximum Displacement	500 μm
Dynamic Characteristic Tester	Maximum Test Frequency	250 kHz
	Maximum Velocity	1.7 m/s
	Maximum Acceleration	14,500 m/s^2
Stiffness Tester	Load Application Range	10–5000 N
	Loading Rate Range	0.001–500 mm/min

Table 2. Main Engine Parameters.

Parameter	Value
Engine type	6 cylinders, water-cooled, Turbocharger with air intercooler
Displacement (L)	5.7
Bore × stroke (mm)	98 × 126
Compression ratio	23:1
Maximum power (kW)	194 @ 2500 rpm
Fuel injection system	Common rail
Number of nozzle holes	8
Diameter of nozzle hole (mm)	0.209

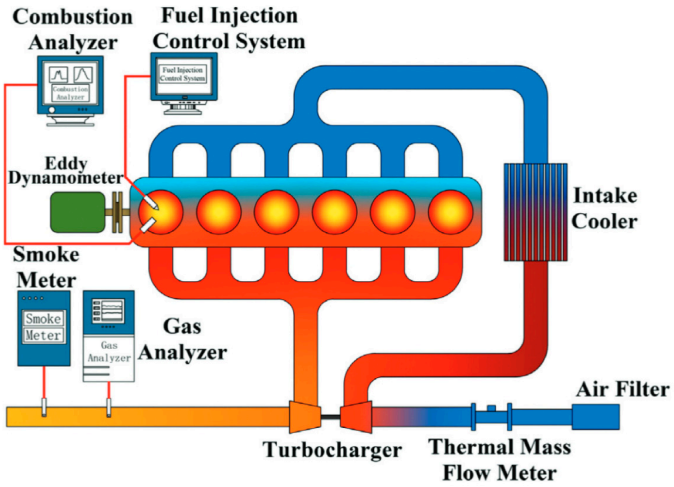


Figure 1. Experimental setup diagram.

The gaseous emissions of the engine were quantified using a Horiba MEXA 7100DEGR gas analyzer and a Fourier transform infrared spectrometer (FTIR), measuring both regular and unregular emissions, respectively. Methanol fuel consumption was measured using a modified AVL 733S fuel flow meter.

The lubricating oil was maintained at a constant temperature of 110 ± 2 °C, while the cooling water was kept at a steady temperature of 85 ± 2 °C to ensure optimal engine performance. Data were collected after the engine had been stabilized for 3 min under

each test condition, and each measurement was repeated three times with the average value reported.

2.2. Fuel Characteristics

In this study, the test fuel employed was chemically pure methanol with a purity of 99.5%, blended with 1000 ppm of a lubricity improver AFTON HiTEC® 4140F (Afton Chemical Corporation, Richmond, VA, USA) to enhance the lubricity of the methanol fuel [29–31]. The characteristics of the methanol fuel used in the study are shown in Table 3.

Table 3. Main properties of methanol and diesel.

Properties	Methanol	Diesel
Cetane number	3–5	51
Lower heating value (MJ/kg)	19.7	42.9
Latent heat of evaporation (kJ/kg)	1110	~232
Boiling point (°C)	64.6	180–370
Viscosity (mm^2/s) at 20 °C	0.58	3.8
Density (kg/m^3) at 20 °C	790	834

2.3. Test Conditions

In light of the preceding analysis highlighting the stringent demands imposed by pure methanol CI engines on fuel injection systems—particularly in terms of dynamic response, drive control strategies, and long-term durability—and addressing the critical bottlenecks of existing commercial piezoelectric injectors when fueled with methanol, namely inadequate transient response and internal flow passage geometries not optimized for the high volumetric flow rates required by methanol combustion, this study undertakes targeted systematic optimizations. Notably, to enhance reliability, the injector material was upgraded to martensitic stainless steel. Following the performance optimizations in this study, the flow rate deviation of the injector remained within 4% after 60 million methanol injection cycles. Comprehensive investigations into long-term durability and reliability will be conducted in future work.

First, this study focused on the coordinated optimization of key components within the piezoelectric injector, specifically targeting the piezoelectric actuator, drive waveform, nozzle seat geometry, and the geometric profile of the displacement-amplifying piston in the internal hydraulic amplifier.

Subsequently, to validate the effectiveness of these modifications, the optimized injector was integrated into a pure methanol CI engine for bench testing. Engine tests were conducted at two selected operating points—1500 r/min with brake mean effective pressures (BMEP) of 0.5 MPa and 1.5 MPa—under identical injection strategies for both the baseline and optimized injectors. By comparing the BSFC and emission characteristics before and after the optimization, the efficacy of the proposed improvements in enhancing engine performance and reducing emissions was systematically evaluated.

Ultimately, this work aimed to overcome existing technical limitations, providing a practical and viable pathway for the engineering implementation of pure methanol CI technology and facilitating the large-scale adoption of methanol fuel in CI engines.

3. Results and Discussions

3.1. Co-Optimization of the Key Structural Design and Control Strategy for the Injector

Targeted optimizations of key components of the piezoelectric injector—namely, the piezoelectric actuator, drive waveform, nozzle seat geometry, and the geometric profile of

the displacement-amplifying piston within the internal hydraulic amplifier of the piezoelectric injector—are presented in this section.

3.1.1. Optimization and Improvement of the Piezoelectric Actuator

This section focused on the optimization of the piezoelectric actuator, with particular emphasis on enhancing the accuracy of its maximum displacement output, response repeatability, and dynamic operational stability—critical performance attributes for high-precision fuel injection control. To ensure that the actuator delivered a highly accurate and consistent maximum displacement upon each electrical activation, this study conducted a refined optimization of the actuator's cross-sectional geometry, the piezoelectric ceramic layer thickness and surface quality.

Figure 2 showed the output displacement of piezoelectric actuators with different sizes of square cross-section under various loading conditions. From the perspectives of load-carrying capacity, operational stability, and manufacturing cost, the 7 × 7 square cross-section demonstrates superior engineering applicability compared to the 5 × 5 configuration.

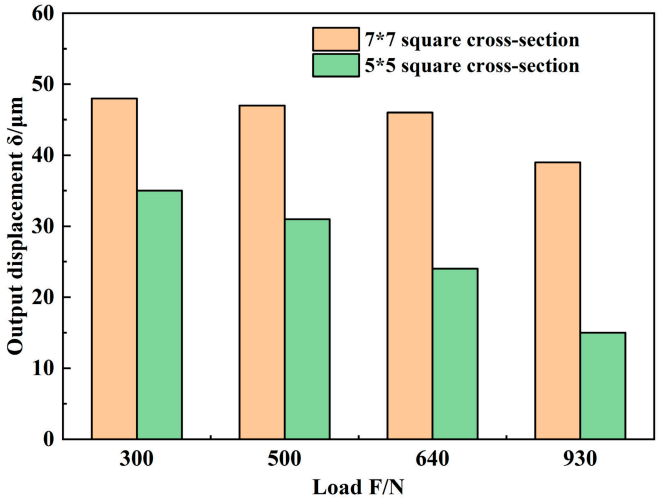


Figure 2. Output displacement versus applied load for different sizes of square cross-section actuators.

Under identical axial loads ranging from 300 N to 930 N, the 7 × 7 design consistently delivered significantly higher output displacement—for instance, approximately 46 μm versus 24 μm at 640 N—and exhibited a slower rate of displacement degradation with increasing load. This indicated a more balanced structural stiffness that enabled greater effective stroke under high backpressure conditions typical in HPCR systems. Consequently, the actuator maintained robust performance against fuel-induced counterforces, preventing insufficient injection quantity or response lag during transient load spikes, thereby fulfilling the stringent "high drive force-large stroke" synergy required by modern high-power-density engines.

The enhanced stability of the 7 × 7 cross-section stems from its larger area, which promotes more uniform stress distribution and effectively mitigates stress concentration—particularly at critical regions such as corners and the transition zone near fixed supports. Additionally, the increased structural mass provided higher inherent damping, which helped suppress high-frequency vibration transmission and minimized displacement oscillations. In contrast, the 5 × 5 design tended to exhibit nonlinear stiffening under elevated loads, leading to degraded displacement repeatability and reduced durability over extended operation, making it less suitable for high-reliability fuel injection applications.

Regarding manufacturability and cost, although the 7 × 7 geometry incurs a material volume increase of approximately 96% compared with the 5 × 5 variant, its straightforward square cross-sectional geometry eliminates the need for complex curved surfaces or tight-tolerance annular fits. It can be efficiently fabricated via standard processes such as wire electrical discharge machining or stamping, significantly simplifying tooling and assembly. Conversely, while the 5 × 5 design uses less raw material, achieving comparable performance necessitates precision preloading mechanisms and high-accuracy guiding structures to compensate for its excessive stiffness—thereby increasing assembly complexity, calibration effort, and scrap rates. In mass production, the 7 × 7 solution proves more cost-effective overall due to its process robustness, higher yield, and lower post-assembly tuning requirements.

In summary, the 7 × 7 square cross-section achieved an optimal trade-off: it moderately increased raw material usage to substantially enhance load resilience and system stability while simultaneously reducing total manufacturing cost through process simplification. This made it particularly well-suited for scalable, high-reliability piezoelectric injector development in advanced internal combustion engine applications.

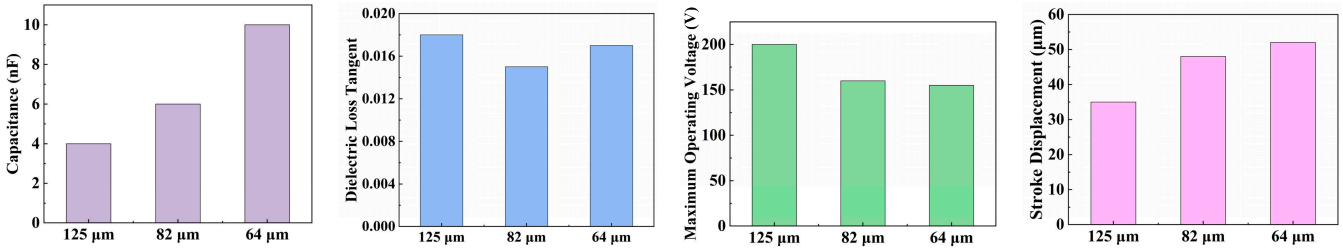
Taking into account the operational requirements of piezoelectric actuators in HPCR fuel injection systems, this study conducted a comparative experimental investigation on specimens with single-layer piezoelectric ceramic thicknesses of 125 μm, 82 μm, and 64 μm, respectively, as shown in Figures 3 and 4. The results indicated that although the 125 μm configuration exhibited a relatively high maximum operating voltage (approximately 200 V), its maximum displacement output was only about 35 μm, which was insufficient to meet the stroke demand for high-dynamic fuel flow modulation. Conversely, the 64 μm configuration achieved a larger displacement (~52 μm) but suffered from a reduced breakdown voltage of approximately 155 V, posing a risk of electrical failure under typical automotive power supply transients and thereby compromising long-term reliability. In contrast, the 82 μm piezoelectric layer achieved an optimal trade-off between maximum operating voltage (160 V) and displacement output (48 μm)—providing adequate electrical safety margin for compatibility with standard automotive drive platforms while delivering sufficient and stable mechanical stroke for direct valve actuation. Consequently, a single-layer thickness of 82 μm was identified in this study as the preferred design choice, balancing safety, actuation performance, and engineering practicality for high-precision, high-reliability piezoelectric injectors.



(**a**) 125 μm (**b**) 82 μm (**c**) 64 μm

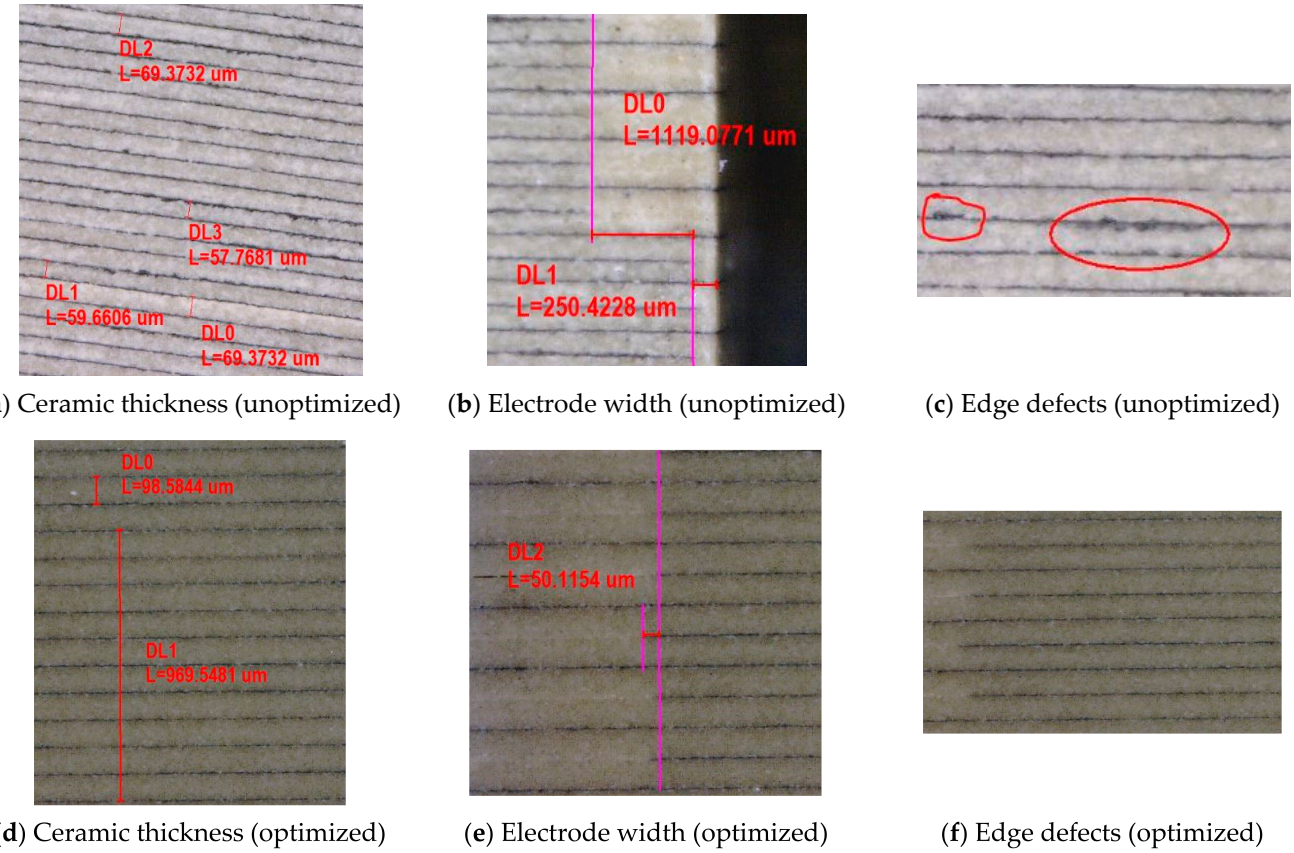
Figure 3. Diaphragm Samples with Varying Thicknesses.

Piezoelectric actuators employed in HPCR fuel injection systems frequently fail due to localized electro–thermo–mechanical coupling instability, with surface quality defects serving as a primary trigger. The surface morphology and conductive architecture of the piezoelectric layers were systematically optimized as shown in Figure 5.



(**a**) Capacitance (**b**) Dielectric loss tangent (**c**) Maximum operating voltage (**d**) Stroke displacement

Figure 4. Influence of Single-Layer Piezoelectric Thickness on Key Actuator Performance Metrics.



(**a**) Ceramic thickness (unoptimized) (**b**) Electrode width (unoptimized) (**c**) Edge defects (unoptimized)

(**d**) Ceramic thickness (optimized) (**e**) Electrode width (optimized) (**f**) Edge defects (optimized)

Figure 5. Comparison of piezoelectric layer surface morphology before (**top**) and after (**bottom**) optimization.

Firstly, non-uniform ceramic thickness (with a deviation of up to 16.7%) induced spatially heterogeneous electric field distribution. The electric field intensity became significantly amplified in locally thinner regions under identical driving voltage ($E = V/d$), creating so-called "electric field hotspots" that readily initiated dielectric breakdown. Concurrently, abrupt thickness transitions generated stress concentrations—arising from elastic modulus mismatches—which accelerated microcrack nucleation under cyclic electromechanical loading. By implementing refined fabrication processes to achieve thickness uniformity (coefficient of variation < 3%), this work effectively synchronized the spatial coherence of both electric and mechanical stress fields, promoting globally balanced energy dissipation and thereby enhancing overall dielectric strength margin.

Secondly, irregular electrode width and edge defects provoked the edge field enhancement effect. Based on electrostatic boundary conditions, the electric field at sharp electrode corners or notches can be amplified by a factor of 3–5, which readily triggers localized air ionization and micro-discharges. Over time, this cumulative damage leads to insulation degradation and eventual short circuits. Through high-precision patterning processes,

geometric regularization of the electrodes not only suppressed field distortion at edges but also fundamentally mitigated the nonlinear growth of leakage current, thereby substantially improving electrical stability under dynamic drive conditions.

3.1.2. Precise and Stable Control of Driving Waveform

During previous experimental testing, a high-voltage "droop" phenomenon was observed in the piezoelectric actuator. Specifically, the actual voltage applied across the actuator terminals consistently fell slightly below the theoretically commanded drive voltage. This discrepancy became increasingly pronounced after prolonged operation under high-load conditions. This phenomenon primarily stemmed from the increased dielectric loss and capacitance drift of the piezoelectric ceramic material under elevated temperatures and high-frequency electric fields. Experimental measurements showed that the actuator capacitance increased from 1 μF to 4.5 μF. This drastic capacitance drift, accompanied by increased dielectric loss at elevated temperatures, led to a significant rise in equivalent series resistance, thereby resulting in greater energy dissipation and voltage drop during drive pulses. Consequently, the displacement output accuracy of the actuator—and ultimately the injection quantity stability—was adversely affected. To address the aforementioned issues, a multi-dimensional coordinated control strategy for precise and stable drive waveform regulation was developed in this study, which was rigorously validated through a series of experiments and simulations.

The first component is the hardware-based energy compensation mechanism. To address the voltage droop issue, a dual-mode high-voltage turn-off feedback circuit was developed (hardware block diagram shown in Figure 6). HV Turn-Off Feedback A operates under normal conditions: it immediately disconnects the high-voltage supply upon detecting completion of charge injection into the piezoelectric actuator, thereby eliminating unnecessary MOSFET conduction losses and improving overall energy efficiency. HV Turn-Off Feedback B serves as a protection and compensation mechanism for abnormal operating conditions, featuring a higher activation threshold. It is triggered when—despite an extended drive pulse width and the actuator voltage having reached its calibrated level—the engine speed remains persistently below the target value. In such cases, the system identifies insufficient actuator output force and signals the MCU to suspend the pulse-width-based over-compensation strategy, thereby preventing excessive stress that could otherwise degrade actuator longevity. As clearly illustrated by Cadence simulations in Figure 7a,b, without compensation the drive voltage exhibited severe droop, collapsing from 200 V to approximately 100 V. In contrast, with the compensation scheme enabled, the drive voltage was successfully maintained at 200 V, effectively ensuring the required actuator displacement—albeit with a slight increase in opening delay. The experimentally measured drive waveforms indicated that the voltage drop induced by dielectric loss was approximately 25 V, which was reduced to less than 5 V after optimization compensation.

Subsequently, a software-based adaptive regulation strategy was implemented. At the software level, a proportional-integral-derivative (PID) feedback control algorithm based on engine speed deviation was employed to dynamically adjust the injection pulse width, with a simplified schematic of the PID structure shown in Figure 8. The MCU continuously sampled the target and actual engine speed signals, and the resulting speed error was converted via an analog-to-digital (A/D) converter and fed back to the control source, enabling servo-level regulation of the injection pulse width. This approach provided precise compensation for minor fueling deviations caused by dielectric losses in the piezoelectric actuator while strictly respecting the actuator's maximum allowable drive voltage, thereby significantly enhancing system robustness and control accuracy. Furthermore, the drive logic was optimized as illustrated in Figure 9, where V_1 denotes the

drive voltage waveform, t_1 represents the initial charging time, t_2 the injection pulse width, t_3 the discharge duration, and t_4 the cylinder selection interval. With drive compensation enabled, the extended charging time—combined with variations in piezoelectric material characteristics—necessitated sustained high-voltage maintenance. Thus, the original charging phase and injection pulse were merged into a unified high-voltage hold period, while t_2 was redefined as a transitional interval between charge and discharge phases to ensure operation remains within safe voltage thresholds, thereby stabilizing the drive voltage waveform.

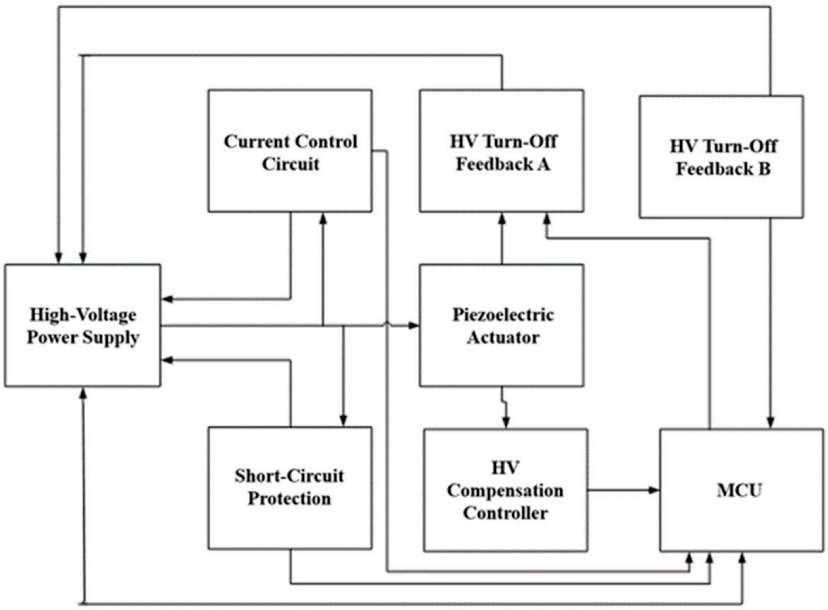
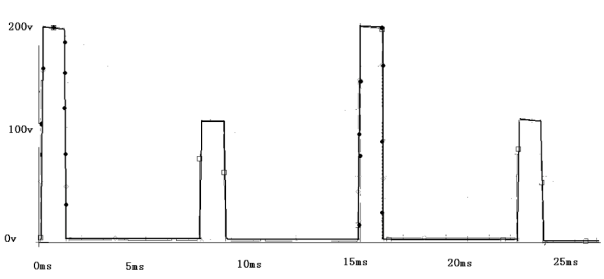
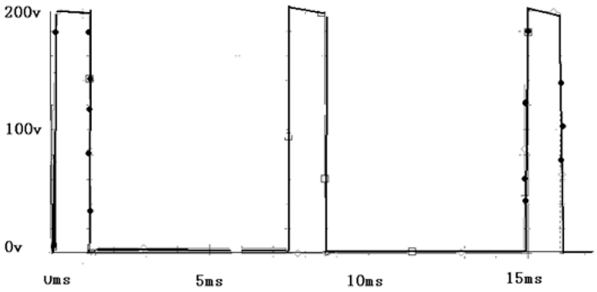


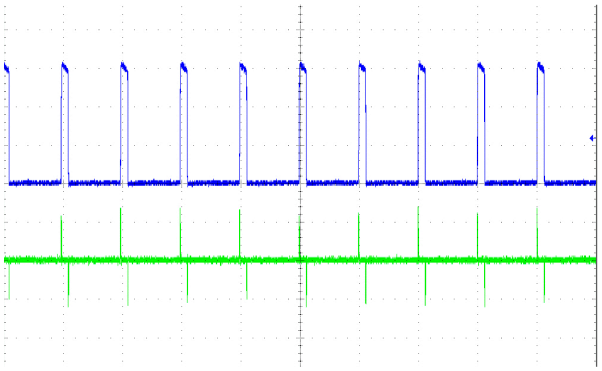
Figure 6. Hardware Block Diagram of the Drive Compensation Circuit.



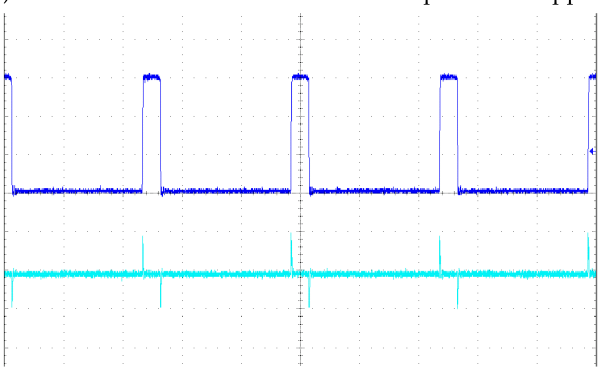
(**a**) Simulated Drive Waveform with Dielectric Loss



(**b**) Simulated Drive Waveform with Compensation Applied



(**c**) Measured Drive Waveform with Dielectric Loss



(**d**) Measured Drive Waveform with Compensation Applied

Figure 7. Simulated and measured Drive Waveform.

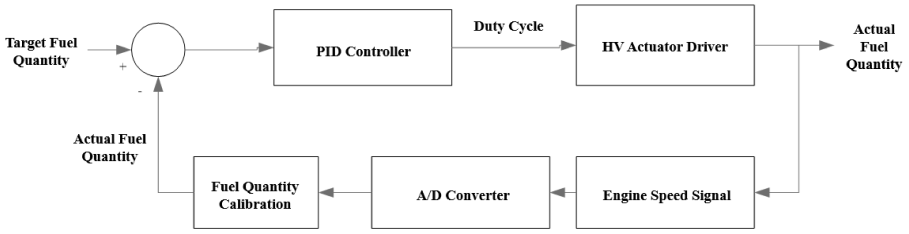
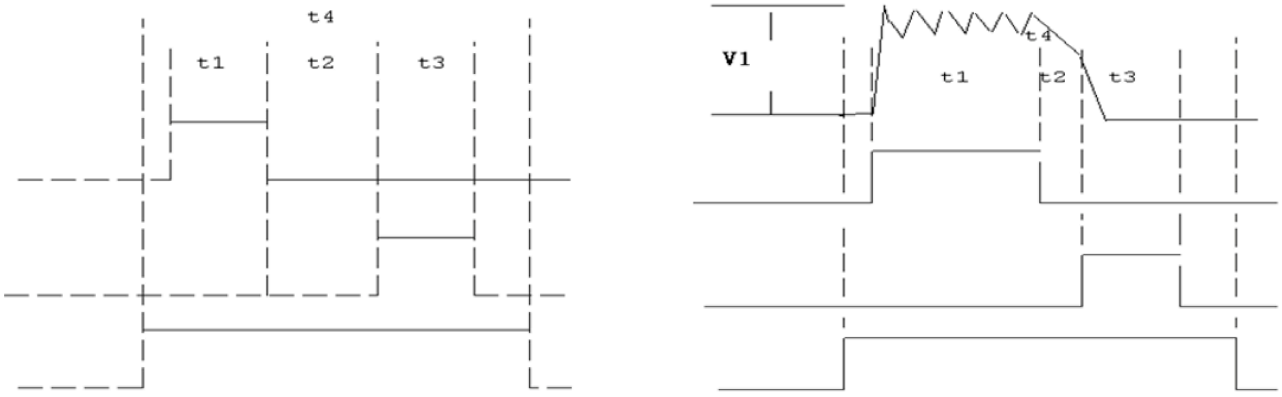


Figure 8. PID Control Structure for Fuel Quantity Compensation.



(**a**) Drive Logic Signal Without Compensation (**b**) Drive Logic Signal With Compensation Implemented

Figure 9. Comparison of Drive Logic Signals with and without Fuel Quantity Compensation.

Furthermore, experimental investigations on current closed-loop control revealed that both the magnitude and stability of the drive current directly influenced the displacement response speed and precision of the piezoelectric actuator. Increasing the drive current significantly enhanced displacement and reduced pressurization time. However, excessive current surges can induce severe displacement oscillations during initial charging and final discharge phases. To address this, the conventional latch-based PWM modulation scheme was replaced with a dual-threshold current control strategy. The first threshold was set to 10 A to limit the inrush current impact during the pre-charge phase, while the subsequent thresholds were set to 15 A to ensure sufficient driving capability. This approach generated high-precision dynamic duty cycle signals via real-time current sensing and feedback, thereby establishing a voltage–current dual closed-loop control system. The proposed strategy effectively suppressed oscillations, achieved higher precision in dynamic duty cycle regulation, improved effective switching efficiency, and reduced switching losses. Consequently, the actuator charging time was reduced from 100 μs to 80 μs, and the resulting drive waveform exhibited high conformity with industry standards.

In addition, comprehensive system-level EMC design measures were implemented at the PCB layout stage to mitigate strong electromagnetic interference generated by the high-voltage, high-current actuation process. These include partitioning the ground plane into separate power and digital domains—interconnected via ferrite beads and zero-ohm resistors at connector interfaces to block noise coupling paths—as well as deploying localized bulk capacitors and current-limiting inductors near critical circuits to confine transient currents and minimize ground bounce and radiated emissions. Additional ferrite beads and decoupling capacitors were placed in sensitive regions. Although these precautions reduced PCB area utilization to approximately 65%, they were essential trade-offs to ensure the safety of high-voltage/high-current networks and guarantee overall system electromagnetic compatibility and operational reliability.

3.1.3. Optimization of Injector Flow Characteristics

Due to the lower heating value (LHV) of methanol (approximately 48% that of diesel), significantly higher fuel mass per cycle is required to achieve equivalent power output, particularly under medium- to high-load operating conditions. Under these circumstances, the maximum flow capacity of the injector becomes a critical bottleneck limiting the reduction in injection pulse width. Excessively long pulse widths not only promote inhomogeneous mixture formation and localized rich zones but also exacerbate wall-wetting and formaldehyde emissions, ultimately degrading BTE. Consequently, enhancing the injector's peak flow rate is essential to enabling high-efficiency, clean combustion in methanol CI engines. To address this requirement, the core flow passages within the hydraulic amplification mechanism of the piezoelectric injector were optimized in this section, with the objective of simultaneously enhancing flow capacity and cavitation resistance while preserving sealing integrity and dynamic response.

The internal structure schematic of the piezoelectric injector is shown in Figure 10. The area within the red circle is the displacement-amplifying piston. Specifically, two key geometric modifications were implemented in the displacement-amplifying piston and the valve seat region: (1) The original conical tip of the displacement-amplifying piston was replaced with a stepped cylindrical profile (Figure 11). This change eliminated abrupt flow area transitions during valve opening, thereby mitigating localized high-velocity jets and low-pressure zones that trigger cavitation erosion—enhancing component durability and manufacturing repeatability. (2) The valve seat geometry was recontoured to increase the minimum flow diameter between the valve spool and seat from 1.3 mm (baseline) to 1.5 mm. This enlargement significantly improved early-stage flow responsiveness: during the initial phase of valve opening, fuel discharge through the outlet orifice rose more rapidly and smoothly with spool travel, eliminating the flow-establishment lag observed in the original design. Combined with streamlined flow path features, these modifications collectively reduced flow losses and pressure oscillations, establishing a robust structural foundation for stable, high-flow-rate methanol injection under medium- to high-load conditions. Experimental flow characterization demonstrated that the optimized injector delivered a flow rate of 2.4 L/min at 100 bar injection pressure, corresponding to a 20.8% improvement over the original configuration. At the maximum injection pressure of 1000 bar for methanol high-pressure direct injection, the flow rates before and after optimization were 6.0 L/min and 7.6 L/min, respectively.

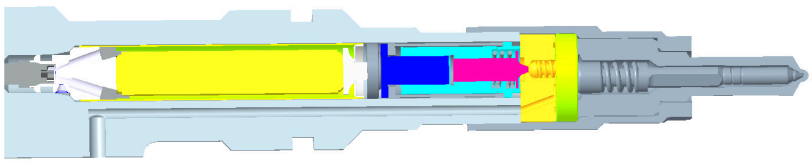
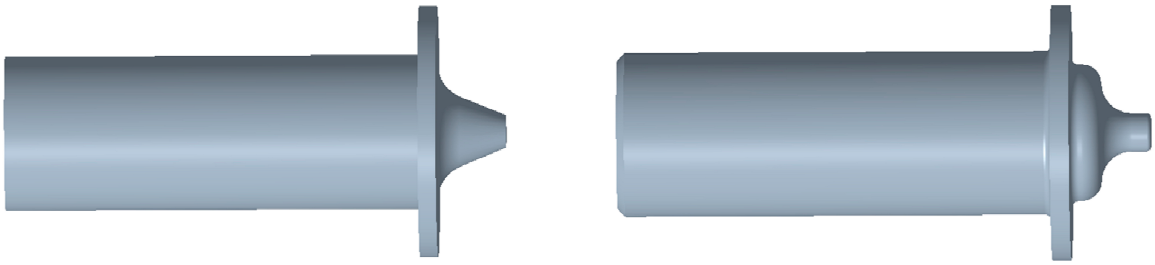


Figure 10. The internal structure schematic of the piezoelectric injector.



(**a**) Displacement-amplifying piston with conical tip (**b**) Displacement-amplifying piston with stepped cylindrical tip

Figure 11. Geometric comparison of the displacement amplification piston pre- and post-optimization.

Figure 12 presents the spray test results of the optimized piezoelectric injector under identical operating conditions. Compared with the baseline injector, the optimized design demonstrated marked improvements in spray characteristics. Notably, the enhanced dynamic response and stable needle lift significantly improved the consistency across different nozzle orifices, resulting in highly symmetrical spray plumes with uniform and extended penetration, while the increased effective flow area yielded a higher mass flow rate. Moreover, air entrainment between adjacent plumes was effectively promoted, resulting in higher gas utilization efficiency within the inter-plume region and a considerable reduction in locally fuel-rich zones. Consequently, overall mixture homogeneity was improved, validating the effectiveness of the optimizations in addressing spray deficiencies.

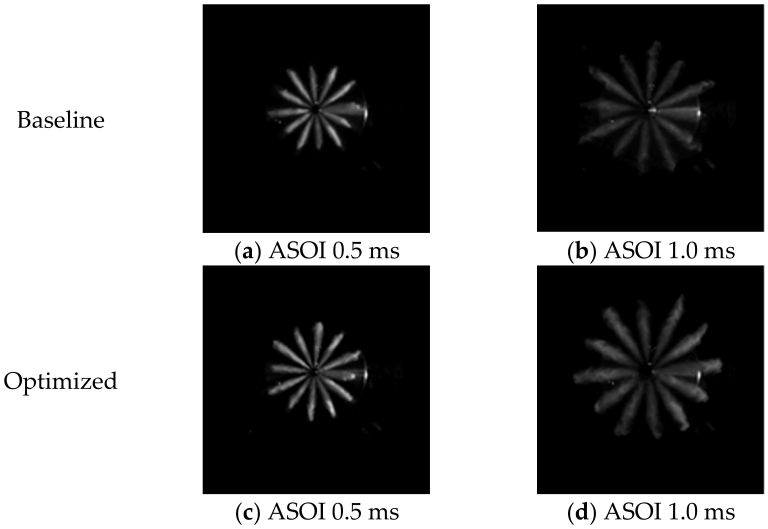


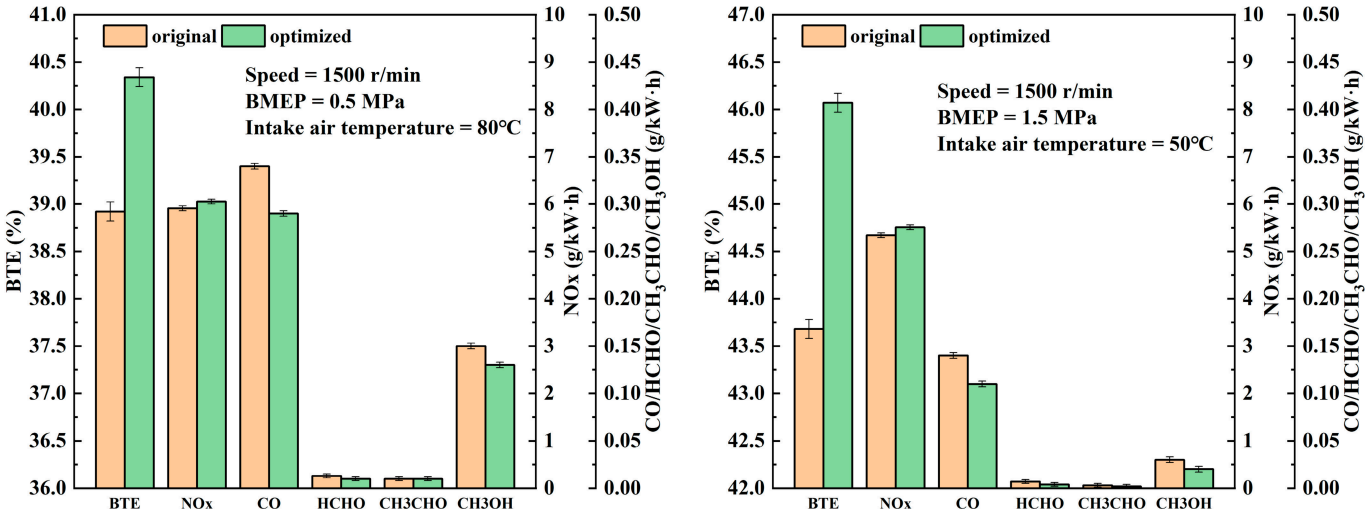
Figure 12. Spray Characterization of the baseline and the optimized Injector.

3.2. Performance and Emission Characteristics of the Engine with the Optimized Injector

A comparative analysis of engine performance and emissions was presented in this section, as shown in Figure 13, with identical injection strategies applied across different injectors. Under the test condition of 1500 r/min, BMEP = 0.5 MPa, and an intake temperature of 80 °C, the optimized injector—benefiting from significantly improved transient response characteristics and enhanced maximum flow capacity achieved in prior development—enabled more precise and rapid fuel delivery control. This allowed for a reduced injection pulse width under the same cyclic fuel demand, resulting in higher initial spray momentum, faster spray penetration, and accelerated droplet breakup and vaporization rates. Consequently, a more homogeneous and timely combustible mixture was formed prior to the main combustion phase, effectively mitigating local rich zones and wall-impingement-induced liquid film accumulation [46]. As a result, the combustion process became more concentrated near top dead center, with an increased peak heat release rate and advanced combustion phasing, directly contributing to an improvement in BTE from 38.9% to 40.4%.

In terms of emission characteristics, with the exception of a marginal 2.37% increase in NO_x, hydrocarbon-related pollutants—including CO, formaldehyde (HCHO), unburned methanol (CH_3OH), and acetaldehyde (CH_3CHO)—exhibited synergistic reductions or remained stable. This behavior profoundly reveals the global regulatory mechanism of spray optimization on the methanol oxidation reaction pathway. The trade-off between NO_x and CO emissions serves as the primary thread for understanding this process. Specifically, NO_x emissions increased from 5.91 to 6.05 g/kW·h, attributed to more concentrated heat release and slightly elevated peak temperatures resulting from enhanced premixing,

which promotes thermal NO_x formation. However, constrained by the inherently low adiabatic flame temperature of methanol, this increment is minimal and represents an acceptable penalty for achieving high-efficiency combustion. Conversely, CO emissions decreased substantially by 14.7% (from 0.34 to 0.29 g/kW·h). The underlying mechanism lies not only in the mitigation of wall film quenching—a primary source of initial CO generation—via refined atomization, but more critically in the elevation of expansion stroke temperatures due to improved mixture homogeneity. This extends the post-oxidation window for the CO-to-CO_2 conversion and enhances the transport of OH radicals into intermediate species zones, thereby completing the entire oxidation chain. Notably, the concurrent and significant reductions in HCHO and CH_3OH (HCHO decreased by 23.1%, from 0.013 to 0.010 g/kW·h; CH_3OH reduced by 13.3%, from 0.15 to 0.13 g/kW·h) provided direct chemical kinetic evidence supporting the aforementioned CO reduction mechanism. In conventional methanol compression ignition, HCHO acts as a critical intermediate. Its subsequent oxidation to CO is frequently inhibited by local low-temperature and fuel-rich zones, leading to HCHO accumulation and eventual exhaust escape. Meanwhile, unburned methanol primarily originates from over-lean regions at the spray periphery or delayed evaporation of wall liquid films. The optimized injection strategy suppressed wall impingement, accelerated droplet evaporation, and intensified in-cylinder turbulence. On one hand, this shortened the physical preparation time for the liquid-to-vapor phase transition, reducing raw CH_3OH emissions caused by incomplete evaporation. On the other hand, elevated local temperatures facilitated the HCHO-to-CO conversion, allowing carbon flux that would otherwise be "frozen" at intermediate stages to proceed towards CO and ultimately CO_2 [47]. Therefore, the substantial reductions in HCHO and CH_3OH were not isolated phenomena. Furthermore, acetaldehyde (CH_3CHO) emissions remained stable at a low level of 0.01 g/(kW·h), exhibiting negligible variation.



(**a**) low load (**b**) high load

Figure 13. Performance and Emission Characteristics of the Engine.

Under the high-load operating condition of 1500 r/min, BMEP = 1.5 MPa, and an intake temperature of 50 °C, the optimized injector enabled precise delivery of the required fuel mass within a shorter injection duration, effectively addressing the common high-load challenges of insufficient spray penetration and delayed air–fuel mixing. The higher instantaneous injection rate promoted finer methanol atomization and faster vaporization, while the improved dynamic response characteristics significantly suppressed wall impingement and liquid film accumulation. This resulted in a more spatially uniform mixture

distribution and a flatter equivalence ratio gradient within the combustion chamber. These enhancements were directly reflected in the combustion process: heat release became more concentrated and combustion duration was shortened, allowing the engine to maintain high energy conversion efficiency even at elevated brake mean effective pressure. Consequently, BTE increased from 43.68% to 46.07%, representing a 5.5% relative improvement. However, the elevated in-cylinder temperatures led to a slight increase in NO_x emissions. In contrast, CO emissions decreased from 0.14 g/kW·h to 0.11 g/kW·h, indicating more complete oxidation. Emissions of HCHO, CH_3CHO, and CH_3OH also exhibited a consistent downward trend, with CH_3OH reduced from 0.03 g/kW·h to 0.02 g/kW·h, further corroborating the reduction in residual fuel and improved combustion completeness attributable to enhanced injector responsiveness and stability. Under high-load conditions, the synergistic optimization of injector responsiveness and flow capacity not only fulfilled the demand for power output but also achieved concurrent improvements in efficiency and combustion cleanliness through intensified air–fuel mixing and combustion coupling [46,47].

Notably, the coefficient of variation (CoV) of IMEP is 2.2% at a BMEP of 0.5 MPa and decreases to 1.2% at a BMEP of 1.5 MPa. Thanks to the synergistic optimization of both the injector design and injection strategy, the CoV values remained consistently low across all tested operating conditions.

4. Conclusions

In this study, a methanol-specific piezoelectric injector was successfully developed and validated through a systematic co-optimization of its actuator, drive strategy, and internal flow geometry, effectively addressing the challenges posed by methanol's low cetane number and energy density. The main conclusions were summarized as follows:

(1) Comprehensive Enhancement of Piezoelectric Injector Core Performance: A multi-faceted optimization strategy was implemented to significantly improve the injector's dynamic response, operational stability, and maximum flow capacity. The actuator was optimized by selecting a 7 × 7 square cross-section and an 82 μm piezoelectric ceramic layer thickness, achieving an optimal balance between high load-bearing capacity (39 μm displacement at 930 N), excellent linearity, and cost-effective manufacturability. To ensure stable and precise control, a sophisticated drive strategy was developed, combining a hardware-based high-voltage energy compensation circuit with a software-based proportional-integral-derivative adaptive regulation algorithm and dual-threshold current closed-loop control. This integrated approach successfully mitigated the high-voltage "droop" phenomenon and reduced the actuator's charging time from 100 μs to 80 μs. Furthermore, the internal flow path was optimized by redesigning the displacement-amplifying piston with a stepped cylindrical profile and enlarging the valve seat's minimum flow diameter. These modifications increased the injector's flow rate by 20.8% to 2.4 L/min at 100 bar, ensuring sufficient fuel supply for all engine operating conditions.

(2) Significant Improvements in Engine Efficiency and Emission Characteristics: Rigorous engine bench testing confirmed that the upgraded injector substantially enhanced both performance and emissions. At low load (Brake mean effective pressure = 0.5 MPa), the Brake thermal efficiency improved from 38.9% to 40.4%. At high load (Brake mean effective pressure = 1.5 MPa), Brake thermal efficiency saw a remarkable increase from 43.68% to 46.07%. These gains were attributed to the injector's superior dynamic performance, which enabled more precise fuel delivery, leading to better spray penetration, faster vaporization, and a more homogeneous air–fuel mixture. Consequently, combustion became more concentrated and complete, resulting in significant reductions in emissions of CO, HCHO, CH_3CHO, and CH_3OH. The only trade-off observed

was a slight increase in NOx emissions, which was a direct consequence of the higher peak combustion temperatures.

(3) Validation of the Co-optimization Strategy for Methanol compression-ignition Engines: The results conclusively demonstrate that the integrated co-optimization of the actuator hardware, drive control logic, and internal flow geometry was a highly effective and practical engineering solution for enabling pure methanol compression ignition. This approach successfully overcame the inherent limitations of methanol fuel by providing the necessary fast response, high flow capacity, and precise control required for stable and efficient combustion. The study provided a robust technical pathway for the large-scale application of pure methanol in compression-ignition engines, highlighting its potential as a viable and clean alternative fuel for future sustainable transportation.

Author Contributions: Conceptualization, Y.W. and H.L.; Methodology, L.Z., M.L. and Y.W.; Validation, H.Z., W.G. and J.L.; Formal Analysis, L.Z. and J.L.; Investigation, M.L., Y.H. and W.G.; Resources, Y.W. and H.L.; Data Curation, L.Z. and M.L.; Writing—Original Draft Preparation, L.Z.; Writing—Review and Editing, Y.W. and H.L.; Visualization, L.Z.; Supervision, Y.W. and H.L.; Project Administration, L.Z.; Funding Acquisition, H.L. All authors have read and agreed to the published version of the manuscript.

Funding: This research was funded by National Natural Science Foundation of China (NSFC) projects of Grant No. U2572204 and. U25A20328.

Data Availability Statement: The study did not report any data.

Conflicts of Interest: All the authors declare that the research was conducted in the absence of any commercial or financial relationships that could be construed as a potential conflict of interest.

References

1. Reitz, D. Directions in internal combustion engine research. *Combust. Flame* **2013**, *160*, 1–8. [CrossRef]
2. Hoseini, S.S.; Najafi, G.; Ghobadian, B.; Mamat, R.; Sidik, N.A.C.; Azmi, W.H. The effect of combustion management on diesel engine emissions fueled with biodiesel-diesel blends. *Renew. Sustain. Energy Rev.* **2017**, *73*, 307–331. [CrossRef]
3. Leach, F.; Kalghatgi, G.; Stone, R.; Miles, P. The scope for improving the efficiency and environmental impact of internal combustion engines. *Transp. Eng.* **2020**, *1*, 100005. [CrossRef]
4. Yue, Z.; Liu, H. Advanced research on internal combustion engines and engine fuels. *Energies* **2023**, *16*, 5940. [CrossRef]
5. Cernat, A.; Pana, C.; Negurescu, N.; Nutu, C.; Lazaroiu, G. An Overview on Pollutant Emissions of Internal Combustion Engines. In *Energy Transition Holistic Impact Challenge (ETHIC): A New Environmental and Climatic Era*; Springer: Cham, Switzerland, 2024; pp. 111–128.
6. Huang, H.; Liu, Q.; Wang, Q.; Zhou, C.; Mo, C.; Wang, X. Experimental investigation of particle emissions under different EGR ratios on a diesel engine fueled by blends of diesel/gasoline/n-butanol. *Energy Convers. Manag.* **2016**, *121*, 212–223. [CrossRef]
7. Huang, H.; Liu, Q.; Teng, W.; Wang, Q. The potentials for improving combustion performance and emissions in diesel engines by fueling n-butanol/diesel/PODE3-4 blends. *Energy Procedia* **2017**, *105*, 914–920.
8. Hung, D.L.; Chen, H.; Xu, M.; Yang, J.; Zhuang, H. Experimental investigation of the variations of early flame development in a spark-ignition direct-injection optical engine. *J. Eng. Gas Turbines Power* **2014**, *136*, 101503.
9. Sharma, S.; Agarwal, S.; Jain, A. Significance of hydrogen as economic and environmentally friendly fuel. *Energies* **2021**, *14*, 7389. [CrossRef]
10. Xue, W.; Zhan, Q.; Zhang, Q.; Wu, Z. Spatiotemporal variations of particulate and gaseous pollutants and their relations to meteorological parameters: The case of Xiangyang, China. *Int. J. Environ. Res. Public Health* **2020**, *17*, 1013623.
11. Anderson, R.; Hawkins, E.; Jones, D. CO_2, the greenhouse effect and global warming: From the pioneering work of Arrhenius and Callendar to today's Earth System Models. *Endeavour* **2016**, *40*, 178–187. [PubMed]
12. Filonchyk, M.; Peterson, M.P.; Yan, H.; Gusev, A.; Zhang, L.; He, Y.; Yang, S. Greenhouse gas emissions and reduction strategies for the world's largest greenhouse gas emitters. *Sci. Total Environ.* **2024**, *944*, 173895. [PubMed]
13. Liu, X.; Shakeel, M.R.; Raman, V.; Mohan, B.; Menaca, R.; Viollet, Y.; AlRamadan, A.S.; Cenker, E.; Im, H.G. Assessment of methanol combustion engines in spark ignition, spark-, and glow plug-assisted compression ignition modes. *Appl. Therm. Eng.* **2025**, *280*, 128538. [CrossRef]

14. Veza, I.; Said, M.F.M.; Latiff, Z.A. Progress of acetone-butanol-ethanol (ABE) as biofuel in gasoline and diesel engine: A review. *Fuel Process. Technol.* **2019**, *196*, 106179. [CrossRef]
15. Senousy, M.; Li, F.; Mumford, D.; Gadala, M.; Rajapakse, R. Thermo-electro-mechanical performance of piezoelectric stack actuators for fuel injector applications. *J. Intell. Mater. Syst. Struct.* **2009**, *20*, 387–399.
16. Han, Y.; Moon, B.; Choi, S. Control performance investigation of piezoelectric actuators under variation of external heat environment. *Trans. Korean Soc. Noise Vib. Eng.* **2015**, *25*, 707–713. [CrossRef]
17. Butcher, M.; Davino, D.; Giustiniani, A.; Masi, A. An experimental evaluation of the fully coupled hysteretic electro-mechanical behaviour of piezoelectric actuators. *Phys. B Condens. Matter* **2016**, *486*, 116–120. [CrossRef]
18. Ossart, F.; Meunier, G. Comparison between various hysteresis models and experimental data. *IEEE Trans. Magn.* **2002**, *26*, 2837–2839.
19. Huang, Z.; Lu, H.; Jiang, D.; Zeng, K.; Liu, B.; Zhang, J.; Wang, X. Combustion behaviors of a compression-ignition engine fuelled with diesel/methanol blends under various fuel delivery advance angles. *Bioresour. Technol.* **2004**, *95*, 331–341. [PubMed]
20. Sayin, C.; Ilhan, M.; Canakci, M.; Gumus, M. Effect of injection timing on the exhaust emissions of a diesel engine using diesel–methanol blends. *Renew. Energy* **2009**, *34*, 1261–1269. [CrossRef]
21. Chao, H.-R.; Lin, T.-C.; Chao, M.-R.; Chang, F.-H.; Huang, C.-I.; Chen, C.-B. Effect of methanol-containing additive on the emission of carbonyl compounds from a heavy-duty diesel engine. *J. Hazard. Mater.* **2000**, *73*, 39–54. [PubMed]
22. Yao, C.; Cheung, C.; Cheng, C.; Wang, Y.; Chan, T.; Lee, S. Effect of diesel/methanol compound combustion on diesel engine combustion and emissions. *Energy Convers. Manag.* **2008**, *49*, 1696–1704. [CrossRef]
23. Yao, C.; Pan, W.; Yao, A. Methanol fumigation in compression-ignition engines: A critical review of recent academic and tech-nological developments. *Fuel* **2017**, *209*, 713–732.
24. Wei, L.; Yao, C.; Wang, Q.; Pan, W.; Han, G. Combustion and emission characteristics of a turbocharged diesel engine using high premixed ratio of methanol and diesel fuel. *Fuel* **2015**, *140*, 156–163. [CrossRef]
25. Goeppert, A.; Czaun, M.; Jones, J.-P.; Prakash, G.K.S.; Olah, G.A. Recycling of carbon dioxide to methanol and derived products–closing the loop. *Chem. Soc. Rev.* **2014**, *43*, 7995–8048. [PubMed]
26. Ampah, J.D.; Yusuf, A.A.; Afrane, S.; Jin, C.; Liu, H. Reviewing two decades of cleaner alternative marine fuels: Towards IMO's decarbonization of the maritime transport sector. *J. Clean. Prod.* **2021**, *320*, 128871. [CrossRef]
27. Zincir, B.; Deniz, C.; Tunér, M. Investigation of environmental, operational and economic performance of methanol partially premixed combustion at slow speed operation of a marine engine. *J. Clean. Prod.* **2019**, *235*, 1006–1019. [CrossRef]
28. Shamun, S.; Shen, M.; Johansson, B.; Tuner, M.; Pagels, J.; Gudmundsson, A.; Tunestal, P. Exhaust PM emissions analysis of alcohol fueled heavy-duty engine utilizing PPC. *SAE Int. J. Engines* **2016**, *9*, 2142–2152. [CrossRef]
29. Wu, Y.; Huang, Z.; Liu, H.; Zheng, Z.; Zhang, X.; Jin, C.; Zhang, Z.; Yao, M. Conventional and unconventional gas emissions and particle matter emissions of methanol CI engine with different EHN addition and compression ratios. *J. Energy Inst.* **2024**, *118*, 101924. [CrossRef]
30. Wu, Y.; Wang, C.; Huang, Z.; Wang, W.; Jin, C.; Zhang, Z.; Zhang, X.; Zheng, Z.; Liu, H.; Yao, M. The combustion and emission characteristics of pure methanol as a substitute fuel for compression ignition engines. *Int. J. Green Energy* **2024**, *21*, 3313–3329. [CrossRef]
31. Liu, H.; Zhang, X.; Zhang, Z.; Wu, Y.; Wang, C.; Chang, W.; Zheng, Z.; Yao, M. Effects of 2-ethylhexyl nitrate (EHN) on combustion and emissions on a compression ignition engine fueling high-pressure direct-injection pure methanol fuel. *Fuel* **2023**, *341*, 127684.
32. Zincir, B.; Shukla, P.; Shamun, S.; Tuner, M.; Deniz, C.; Johansson, B. Investigation of effects of intake temperature on low load limitations of methanol partially premixed combustion. *Energy Fuels* **2019**, *33*, 5695–5709. [CrossRef]
33. Svensson, E.; Li, C.; Shamun, S.; Johansson, B.; Tuner, M.; Perlman, C.; Lehtiniemi, H.; Mauss, F. *Potential Levels of Soot, NOx, HC and CO for Methanol Combustion*; SAE Technical Paper; SAE International: Warrendale, PA, USA, 2016.
34. Svensson, E.; Verhelst, S. *Numerical Optimization of Compression Ratio for a PPC Engine Running on Methanol*; SAE Technical Paper; SAE International: Warrendale, PA, USA, 2019.
35. Pucilowski, M.; Jangi, M.; Shamun, S.; Tuner, M.; Bai, X.-S. *The Effect of Injection Pressure on the NOx Emission Rates in a Heavy-Duty DICI Engine Running on Methanol*; SAE Technical Paper; SAE International: Warrendale, PA, USA, 2017.
36. Svensson, E.; Tuner, M.; Verhelst, S. *Influence of Injection Strategies on Engine Efficiency for a Methanol PPC Engine*; SAE Technical Paper; SAE International: Warrendale, PA, USA, 2019.
37. Pucilowski, M.; Fatehi, H.; Jangi, M.; Lonn, S.; Matamis, A.; Andersson, O.; Richter, M.; Bai, X.-S. *Numerical Investigation of Methanol Ignition Sequence in an Optical PPC Engine with Multiple Injection Strategies*; SAE Technical Paper; SAE International: Warrendale, PA, USA, 2019.
38. Aziz, A.; Garcia, A.; Dos Santos, C.P.; Tuner, M. *Impact of Multiple Injection Strategies on Performance and Emissions of Methanol PPC Under Low Load Operation*; SAE Technical Paper; SAE International: Warrendale, PA, USA, 2020.
39. Lu, X.; Wu, T.; Ji, L.; Ma, J.; Huang, Z. Effect of port fuel injection of methanol on the combustion characteristics and emissions of gas-to-liquid-fueled engines. *Energy Fuels* **2009**, *23*, 719–724.

40. Zheng, K.; Dong, X.; Tian, X. Piezomechanics characteristics study of piezoelectric stack actuator. *Mater. Res. Innov.* **2014**, *18*, 132–135. [CrossRef]
41. Zhang, Y.; Tu, Z.; Lu, T.-F.; Al-Sarawi, S. A simplified transfer matrix of multi-layer piezoelectric stack. *J. Intell. Mater. Syst. Struct.* **2017**, *28*, 595–603.
42. Jiang, S.; Cheng, L. Modeling and design of a pre-stressed piezoelectric stack actuator. *AIP Adv.* **2017**, *7*, 331–341. [CrossRef]
43. d'Ambrosio, S.; Ferrari, A. Diesel engines equipped with piezoelectric and solenoid injectors: Hydraulic performance of the injectors and comparison of the emissions, noise and fuel consumption. *Appl. Energy* **2018**, *211*, 1324–1342. [CrossRef]
44. Chung, M.; Kim, J.; Kim, S.; Sung, G.; Lee, J. Effects of hydraulic flow and spray characteristics on diesel combustion in CR direct-injection engine with indirect acting Piezo injector. *J. Mech. Sci. Technol.* **2015**, *29*, 2517–2528. [CrossRef]
45. Taylor, C.; Washington, G. The application of piezoceramic actuation to direct fuel injection. In *Small Engine Technology Conference & Exposition*; SAE Technical Paper; SAE International: Warrendale, PA, USA, 2003.
46. Fettes, C.; Leipertz, A. Potentials of a piezo-driven passenger car common rail system to meet future emission legislations-an evaluation by means of in-cylinder analysis of injection and combustion. In *Spring Fuels & Lubricants Meeting & Exhibition*; SAE Technical Paper; SAE International: Warrendale, PA, USA, 2001.
47. Oki, M.; Matsumoto, S.; Toyoshima, Y.; Ishisaka, K.; Tsuzuki, N. *180 MPa Piezo Common Rail System*; SAE Technical paper; SAE International: Warrendale, PA, USA, 2006.

Disclaimer/Publisher's Note: The statements, opinions and data contained in all publications are solely those of the individual author(s) and contributor(s) and not of MDPI and/or the editor(s). MDPI and/or the editor(s) disclaim responsibility for any injury to people or property resulting from any ideas, methods, instructions or products referred to in the content.